



Spatial-Correlation Based Persistent Scatterer Interferometric Study for Ground Deformation

Kousik Biswas¹ · Debashish Chakravarty² · Pabitra Mitra³ · Arundhati Misra⁴

Received: 9 September 2016 / Accepted: 14 December 2016 / Published online: 16 January 2017
© Indian Society of Remote Sensing 2017

Abstract Interferometric Synthetic Aperture Radar (InSAR), nowadays, is a precise technique for monitoring and detecting ground deformation at a millimetric level over large areas using multi-temporal SAR images. Persistent Scatterer Interferometric SAR (PSInSAR), an advanced version of InSAR, is an effective tool for measuring ground deformation using temporally stable reference points or persistent scatterers. We have applied both PSInSAR and Small Baseline Subset (SBAS) methods, based on the spatial correlation of interferometric phase, to estimate the ground deformation and time-series analysis. In this study, we select Las Vegas, Nevada, USA as our test area to detect the ground deformation along satellite line-of-sight (LOS) during November 1992–September 2000 using 44 C-band SAR images of the European Remote Sensing (ERS-1 and ERS-2) satellites. We observe the ground displacement rate of Las Vegas is in the range of -19 to 8 mm/year in the same period. We also cross-compare PSInSAR and SBAS using mean LOS velocity and time-series. The comparison shows a correlation coefficient of 0.9467 in the case of mean LOS velocity. Along this study, we validate the ground deformation results from the satellite with the ground water depth of Las

Vegas using time-series analysis, and the InSAR measurements show similar patterns with ground water data.

Keywords InSAR · Persistent scatterer · PSInSAR · SBAS · Ground deformation · Spatial correlation

Introduction

Nowadays radar remote sensing is one of the principal applications of the spaceborne satellites and airborne sensors launched over last few decades, especially for studying the hazard-prone or inaccessible areas. Spaceborne SAR was first introduced during the NASA's SEASAT mission in 1978 for remote sensing of ocean applications (Fu and Holt 1982). Afterwards, ESA has launched its first spaceborne SAR ERS-1 in 1991, which contributed the data being available for Interferometric Synthetic Aperture Radar (InSAR). InSAR requires two SAR images of the same area to generate terrain elevation map using the interferogram of the phase data. It can compute the measurement of surface elevation at day/night, all-weather condition, which is one of the advantages of active remote sensing. However, there are problems associated with InSAR caused by the changes in the scatterer of earth's surface with time (Zebker and Villasenor 1992). This leads to loss of interferometric coherence (Hanssen 2001), and signal decorrelation occurs. These decorrelations include temporal, geometric decorrelation and atmospheric artifacts due to variation in atmospheric signal delay. Other known InSAR error sources comprise of residual DEM or topographic and orbital errors, noises like coregistration, unwrapping errors. Deformation measurements are not possible for areas with low coherence. Persistent/Permanent Scatterer InSAR (PSInSAR) masks the InSAR errors

✉ Kousik Biswas
kousikju2012@gmail.com

¹ Advanced Technology Development Centre, Indian Institute of Technology Kharagpur, Kharagpur 721302, India

² Department of Mining Engineering, Indian Institute of Technology Kharagpur, Kharagpur 721302, India

³ Department of Computer Science and Engineering, Indian Institute of Technology Kharagpur, Kharagpur 721302, India

⁴ Space Applications Centre, ISRO, Ahmedabad, India

using stable phase points, also known as PS (Persistent Scatterer) points which remain stable in a stack of SAR images. It overcomes the decorrelation problems of InSAR by identifying certain pixels whose scattering is dominated by one main single scatterer in a series of interferograms.

PSInSAR can be used to detect PS in both urban and non-urban ground areas, especially with vegetation cover where decorrelation is a major problem. During the last decade, PSInSAR studies are mainly based on baseline configuration (single master/multi-master), PS selection criteria, and deformation model. The PSInSAR technique was first developed by (Ferretti et al. 2000, 2001). (Colesanti et al. 2003) proposed an improved PSInSAR based on amplitude dispersion. Other similar methods include Interferometric Point Target Analysis (IPTA) (Werner et al. 2003), Generic SAR Interferometric Software (GENESIS) PSI (Adam et al. 2003), Delft Persistent Scatter Interferometry (DePSI) (Kampes 2005), Spatio-Temporal Unwrapping Network (STUN) algorithm (Kampes and Adam 2006). These methods, based on single master configuration, use the dispersion of amplitude i.e. amplitude variations in a stack of interferograms as a threshold to identify PS. They also rely on a prior deformation model which is linear in time and sometimes referred to as the temporal model of PSInSAR. These techniques can be applied more effectively in urban areas than in non-urban areas, such as natural terrains. (Hooper et al. 2004) developed Stanford Method for Persistent Scatterers (StaMPS), a PSInSAR framework which can successfully detect deformation in both urban and non-urban areas without any prior deformation model in time. This method uses amplitude statistics as well as phase statistics to determine PS based on their phase stability. It is based on the assumption that deformation is spatially correlated or smooth and sometimes called spatial correlation based PSInSAR. CTM (Coherent Target Monitoring) by (Van der Kooij et al. 2005) is another similar method based on the spatial correlation model. More detailed and improved spatially correlated PSInSAR can be found in (Hooper et al. 2007, 2012). PSInSAR methods are based on single-master single-looked interferograms. Small Baseline Subset (SBAS) methods, based on multiple master baseline model, was first introduced by (Berardino et al. 2002). In SBAS methods, a subset of small baseline interferograms is chosen according to the high correlation values to reduce the effect of decorrelation. Generally, multi-looked interferograms are used for SBAS, but can be applied to full-resolution (Lanari et al. 2004). PSInSAR and SBAS are both capable of detecting ground deformations due to groundwater extraction (Ng et al. 2012), urban subsidence (Tesauro et al. 2000), and volcanic deformation (Hooper 2006).

In this study, we have used the PSInSAR and SBAS algorithm of StaMPS (Hooper et al. 2012) framework for

estimation of ground deformation of Las Vegas area using same ERS dataset. The same study area has been used for ground deformation detection in previous studies (Amelung et al. 1999; Bell et al. 2008; Hoffmann et al. 2001) using different methods. We observe the same pattern and magnitude of deformation with the past results. The results of PSInSAR and SBAS were compared using time-series analysis, and finally, both are compared with the USGS groundwater level data for validation. The comparison between PSInSAR, SBAS, and groundwater level results in a good correlation with some discrepancies in long baseline SAR acquisitions. We also statistically compared the mean LOS deformation rate of common PS and SBAS pixels and observed a correlation of 0.9467.

Geological Settings and Data

We chose Las Vegas as our test site, and previous studies (Amelung et al. 1999; Bell et al. 2008; Hoffmann et al. 2001) have reported ground deformation activities in the same area. Las Vegas, a city located in the southern part of the state of Nevada, is one of the populated cities in the US. Being a part of Clark County and Mojave desert, the city is situated in the Las Vegas valley, surrounded by several mountain ranges on all sides. Las Vegas experienced ground subsidence of several feet as a result of aquifer system compaction (Galloway et al. 1999), which contributes to some of the faults running through the city. The region of interest (ROI), draped over the SRTM DEM of Las Vegas, is shown in a red dotted rectangle in Fig. 1.

For this PS and SBAS study, we selected 44 ERS descending images (track 356, frame 2871), shown in red circles in Figs. 2 and 3, captured between April 1992 and February 2000 of Las Vegas city. All the SAR images were processed w.r.t the master or reference image of 13 June 1997. We used 43 single-look interferograms, shown as blue edges in Fig. 2, generated using common master for PSInSAR, and 290 small baseline single-look interferograms, shown as blue edges in Fig. 3, for SBAS analysis. All the ERS SAR images, shown in Table 1, were collected as a raw image (level 0 product) from the archive database.

The Shuttle Radar Topography Mission's (SRTM) DEM (Digital Elevation Model) of 30 m resolution was used for topographic phase correction and geocoding. We cropped the master image (6001 lines \times 1601 pixels) to meet our ROI (approximately 30 km \times 45 km). The perpendicular baselines are within the range of critical baseline (1100 m for ERS). The range, mean, and standard deviation of spatial and temporal baselines are shown in Table 2. We observed no significant temporal gaps except for the year 1994 when "geodetic" and "shifted geodetic" phase have occurred for ERS-1.

Fig. 1 Study area of Las Vegas, superimposed on SRTM DEM, is shown in the dotted red rectangle. The *Inset* map shows the same area located in the southern part of Nevada (colour figure online)

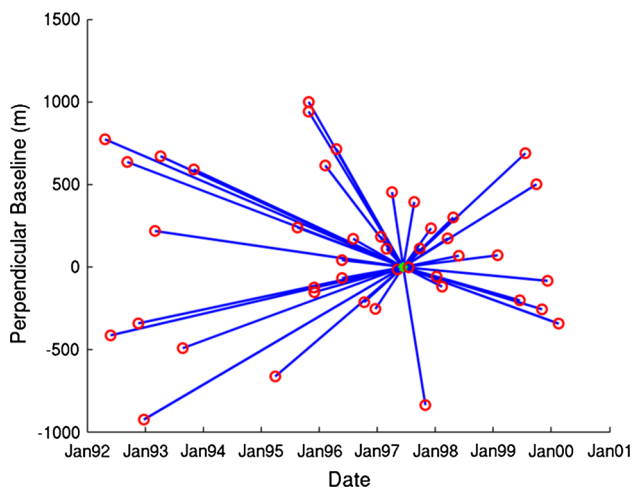
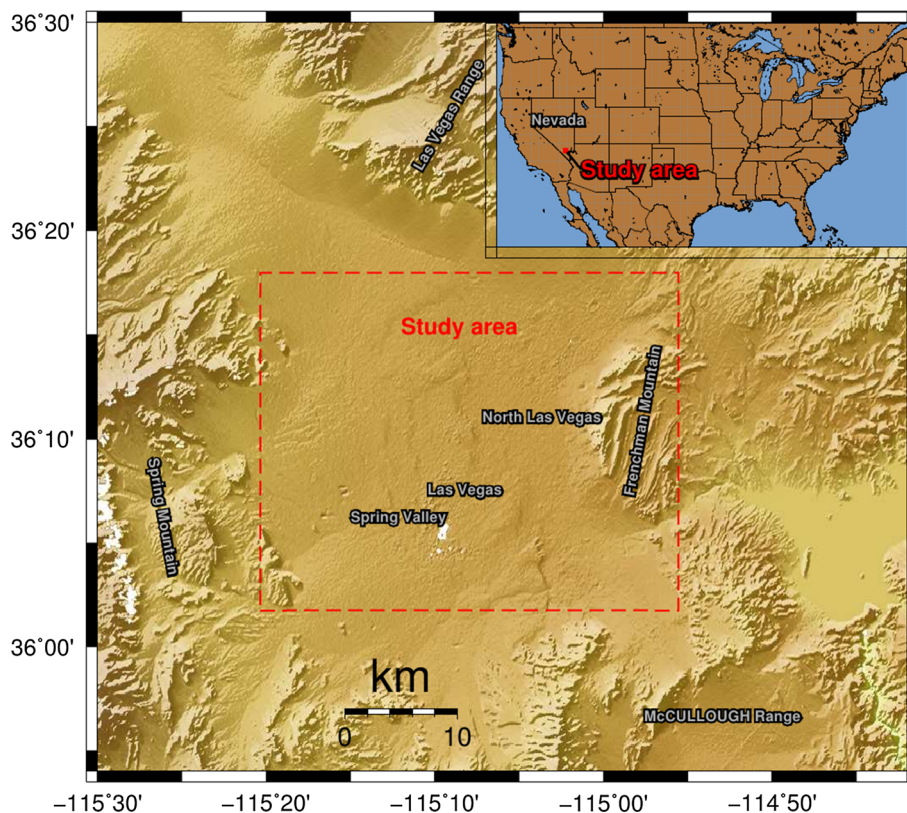


Fig. 2 Perpendicular baseline plots of 44 ERS images (track 356, frame 2871) used for PSInSAR analysis. The master acquisition of 13 June, 1997 is shown in *green asterisk*, the slave images are shown in *red circles*. The *blue lines* denote the 43 interferograms. Here, image acquisition time is depicted along X-axis and perpendicular baseline distance (in meter) is depicted along Y-axis (colour figure online)

PSInSAR Processing

Permanent Scatterer Interferometry or PSI processing algorithms can be roughly divided into two broad categories (1) temporal model of deformation (2) spatial correlation of phase. Temporal model based PSI algorithms assume a

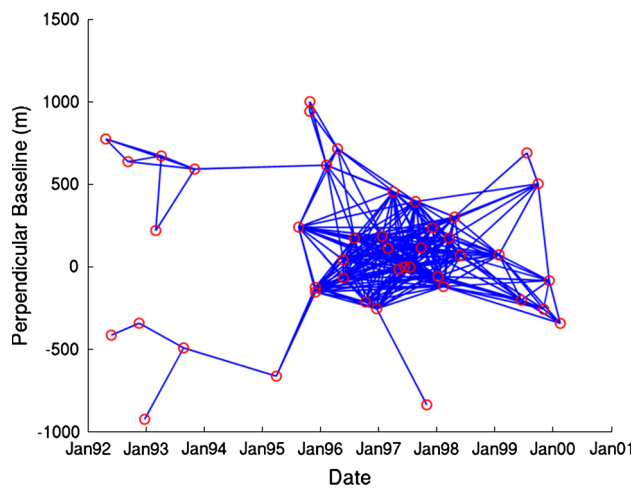


Fig. 3 Small baseline subset plots of all pairs of images (track 356, frame 2871) used in SBAS analysis. The 44 ERS images are shown in *red circles*; the *blue lines* represent the 290 small baseline interferograms used in this study (colour figure online)

linear functional model of deformation (Ferretti et al. 2001; Kampes 2005). Therefore, a prior temporal deformation model is required for measuring ground deformation. On the other hand, spatial correlation based techniques (Hooper et al. 2004; Van der Kooij et al. 2005) relies on the fact that the ground deformation on the earth’s surface is correlated in space up to a certain scale. The spatial correlation method does not need any prior deformation model of ground

Table 1 Details of SAR data used in this study

Sl. no.	Date of acquisition	Perpendicular baseline (m)	Temporal baseline (days)
1	21-Apr-92	775	−1879
2	26-May-92	−414	−1844
3	08-Sep-92	637	−1739
4	17-Nov-92	−341	−1669
5	22-Dec-92	−924	−1634
6	02-Mar-93	219	−1564
7	06-Apr-93	672	−1529
8	24-Aug-93	−491	−1389
9	02-Nov-93	592	−1319
10	30-Mar-95	−663	−806
11	17-Aug-95	240	−666
12	26-Oct-95	943	−596
13	27-Oct-95	1001	−595
14	30-Nov-95	−124	−561
15	01-Dec-95	−152	−560
16	08-Feb-96	616	−491
17	18-Apr-96	715	−421
18	23-May-96	42	−386
19	24-May-96	−67	−385
20	02-Aug-96	172	−315
21	11-Oct-96	−213	−245
22	20-Dec-96	−254	−175
23	24-Jan-97	184	−140
24	28-Feb-97	111	−105
25	04-Apr-97	455	−70
26	09-May-97	−14	−35
27	13-Jun-97	0	0
28	18-Jul-97	−2	35
29	22-Aug-97	395	70
30	26-Sep-97	113	105
31	31-Oct-97	−836	140
32	05-Dec-97	235	175
33	09-Jan-98	−57	210
34	13-Feb-98	−118	245
35	20-Mar-98	174	280
36	24-Apr-98	301	315
37	29-May-98	69	350
38	29-Jan-99	73	595
39	18-Jun-99	−201	735
40	23-Jul-99	690	770
41	01-Oct-99	502	840
42	05-Nov-99	−256	875
43	10-Dec-99	−83	910
44	18-Feb-00	−343	980

The master or reference image is shown in bold

displacements, and it can measure non-steady deformation for both urban and non-urban areas. We have adapted spatial correlation based methodology for PSI processing in our

study as shown in Fig. 4. StaMPS (Hooper et al. 2012), implements spatial correlation based PSI for measuring non-steady ground displacement, generates PS (Permanent

Table 2 Baseline statistics w.r.t master image

	Maximum	Minimum	Mean	Standard deviation
Spatial baseline (m)	1001	2	352	287
Temporal baseline (days)	1879	35	653	564

Scatterer) time-series from SAR images of the same area acquired over different time. StaMPS will work even if man-made artificial structures are not in abundance, where temporal methods may fail to detect PS. It incorporates ROI-PAC (Repeat Orbit Interferometry PACKage) and DORIS (Delft Object-oriented Radar Interferometric Software) for focusing raw SAR image and interferometric processing as a prerequisite. The minimum number of interferograms required for StaMPS PSInSAR processing is 12 (Hooper 2006). The main steps of this approach are given below (Hooper 2006):

Interferometric Processing

Interferogram formation in the case of StaMPS differs from traditional InSAR processing in certain aspects. It generates single-master interferograms of full resolution, which are suitable for PS analysis. PS pixels are not affected by decorrelation; hence no azimuth or range filtering is applied on the Single Look Complex (SLCs).

Selection of Master Image

The selection of the master image depends on the total correlation of interferometric phase (ΣC_{ph}). Depending on the chosen master image, the sum of correlation (ΣC_{ph}), over all interferograms n , may vary. We chose an image as the master image, so that, it maximises the sum of correlation (or minimises the sum decorrelation) of all the interferograms. The correlation (C_{ph}) can be expressed as a product of correlation of four terms, temporal baseline (T), perpendicular baseline (B_{perp}), Doppler centroid baseline (f_{dc}) and thermal noise. The total correlation can be expressed as,

$$C_{ph} = C_{temporal} C_{spatial} C_{doppler} C_{thermal} \approx \left(1 - f\left(\frac{T}{T^c}\right)\right) \left(1 - f\left(\frac{B_{perp}}{B_{perp}^c}\right)\right) \left(1 - f\left(\frac{f_{dc}}{f_{dc}^c}\right)\right) (C_{thermal}) \tag{1}$$

where $f(x) = \begin{cases} 1, & \text{if } x > 1 \\ x, & \text{if } x \leq 1 \end{cases}$ Here, the superscript ‘c’ denotes the critical values for the respective parameters. If the value of spatial or temporal or Doppler baselines is greater the critical value, the total correlation C_{ph} becomes zero. In the case of C-band satellites like ERS, $T^c = 5$ - years, $B_{perp}^c = 1100$ m, $f_{dc}^c = 1380$ Hz in arid regions (Hooper 2006). The “master” image which maximises

$\sum_{k=1}^n C_{ph}$, assuming $C_{thermal}$ as a constant and n is the number of single-look interferograms, is chosen for this study.

Coregistration

Sometimes, interferometric pair with a higher baseline, e.g. spatial, temporal, Doppler, tend to produce high decorrelation and less coherence (<0.2). This is one of the limitations of amplitude based cross-correlation. StaMPS use a modified amplitude based algorithm based on “weighted least-square inversion” for calculating the offset between master and slave image pairs. It allows images with larger baselines to be used than normal InSAR. Slaves with large baselines are not directly coregistered to master; rather, they are coregistered to nearest slaves whose baselines are close to the master.

PS Identification

Stamps PS processing starts with multiple interferograms, which are flat-earth subtracted (geodetic phase correction) and topographically (DEM phase correction) corrected, and they are generated using a single master as the reference. The initial set of PS candidate (PSC) pixels, which are potential candidates for PS, are selected by an amplitude analysis method. Those pixels are chosen for phase analysis to estimate the PS probability in a series of interferograms.

Initial PS Candidate Selection

Amplitude stability of each pixel is estimated using a statistic called amplitude dispersion value (D_A) (Ferretti et al. 2001). Amplitude dispersion index (D_A) can be expressed as, $D_A = \frac{\sigma_A}{\mu_A}$ where σ_A and μ_A are the standard deviation and mean of amplitude vector $A = (A_1 A_2 \dots A_N)$ respectively, where N is the number of images. D_A also can be viewed as a coefficient of variation. The higher the value of D_A , the lower is the amplitude stability of the pixel. (Ferretti et al. 2001) also showed that for a signal having large signal to noise ratio (SNR) D_A becomes phase standard deviation (σ_ϕ) i.e., $D_A \approx \sigma_\phi$. However, for low SNR values, this equivalence relation, between D_A and σ_ϕ , does not hold well. PS candidate selection method uses D_A as a threshold value (typically 0.4–0.42) for each pixel to generate PS candidates.

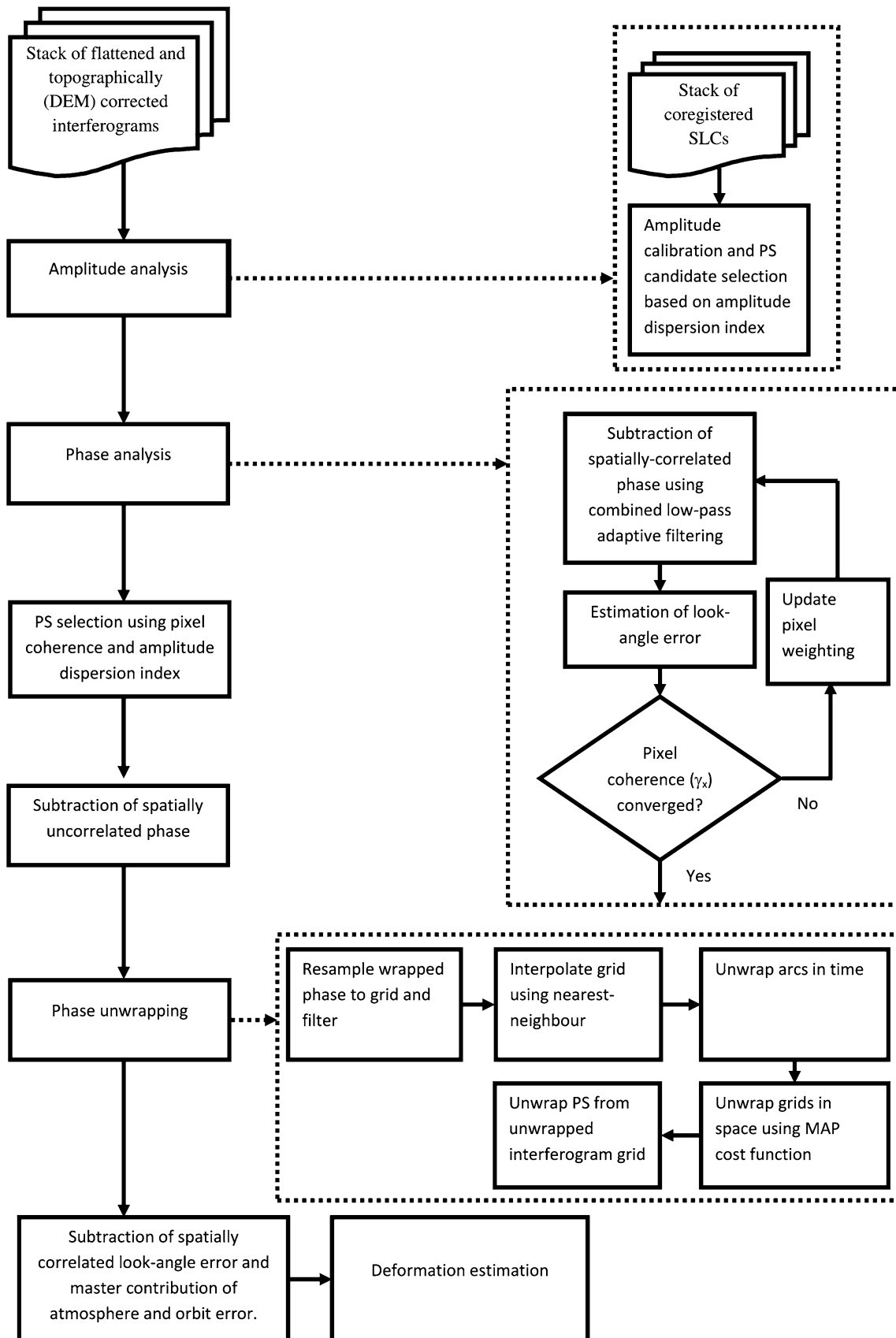


Fig. 4 Flow chart of the StaMPS PSInSAR framework

Phase Analysis of PS Candidates

PS phase analysis is carried out after the initial PS candidate selection in an iterative way. After the amplitude analysis, the phase stability of each PS pixel is measured. The phase of each pixel of “flattened” and topographically corrected interferogram can be expressed as a function of wrapped phase of five terms,

$$\varphi_{interfero,x,i} = W(\varphi_{defo,x,i} + \varphi_{atmo,x,i} + \varphi_{DEM,x,i} + \varphi_{orbit,x,i} + \varphi_{noise,x,i}) \tag{2}$$

where W denotes the wrapping operator, $\varphi_{defo,x,i}$, $\varphi_{atmo,x,i}$, $\varphi_{DEM,x,i}$, $\varphi_{orbit,x,i}$, $\varphi_{noise,x,i}$ denote the phase of x th pixel in the i th interferogram due to deformation, atmospheric artefacts, residual DEM error, orbit position inaccuracy, noise in phase due to thermal effects, co-registration errors etc. respectively. The phase analysis model assumes that the phase due to deformation, atmosphere, part of residual DEM error, and orbital errors are spatially correlated over a certain length. The first four terms on the right-hand side of the equation usually dominate the noise. Hence, the spatially correlated contribution of the four terms (deformation, atmosphere, DEM and orbit) are estimated using an adaptive band-pass filter and subtracted from interferogram phase $\varphi_{interfero,x,i}$. The uncorrelated part of DEM error is estimated using correlation with perpendicular baseline and subtracted from $\varphi_{interfero,x,i}$. The remaining noise term $\varphi_{noise,x,i}$ becomes negligible in the case of PS pixels.

Phase Noise Estimation

After removing the spatially correlated and partially uncorrelated part of the signal, the PS candidate pixels are left with phase noise. The phase stability indicator or temporal coherence estimator Gamma or (γ_x) for pixel x , which indicates whether a pixel is PS, is calculated as follows,

$$\gamma_x = \frac{1}{N} \left(\left(\sum_1^N \exp(j(\varphi_{interfero,x,i} - \overline{\varphi_{interfero,x,i}} - \Delta\varphi_{h,x,i})) \right) \right) \tag{3}$$

where N is the no of interferograms, $j = \sqrt{-1}$, $\overline{\varphi_{interfero,x,i}}$ denotes the estimated spatially correlated part of signal, and $\Delta\varphi_{h,x,i}$ is the estimation of uncorrelated DEM error, γ_x conveys a measure of closeness between the phase of the pixel in a series of interferograms, and it is similar to the concept of coherence value. The phase noise estimation is carried out using iteration on change in γ_x i.e. $\Delta\gamma_x$. Iteration continues until $\Delta\gamma_x$, the difference of γ_x between successive iterations, is below a user-defined threshold value.

PS Selection

It is observed that γ_x and probability of a pixel to be PS is statistically correlated. So, pixels having higher phase stability value are expected to be PS. Here, the probability density of γ_x , $P(\gamma_x)$ is measured by normalising the value of γ_x using the weighted sum of the probability of the pixel is PS and non-PS, $P_{PS}(\gamma_x)$ and $P_{NPS}(\gamma_x)$ respectively. Generally, the candidate pixels having lower phase stability value (γ_x) are down-weighted. $P(\gamma_x)$ is calculated as follows,

$$P(\gamma_x) = \alpha P_{PS}(\gamma_x) + (1 - \alpha) P_{NPS}(\gamma_x) \tag{4}$$

where $0 \leq \alpha \leq 1$, $P_{NPS}(\gamma_x)$ is determined by selecting random phase pixels. When γ_x is lower < 0.3 , $P_{PS}(\gamma_x) \approx 0$ so,

$$\int_0^{0.3} P(\gamma_x) d\gamma_x = (1 - \alpha) \int_0^{0.3} P_{NPS}(\gamma_x) d\gamma_x \tag{5}$$

α can be calculated by putting the data value of $P(\gamma_x)$ and $P_{NPS}(\gamma_x)$ by simulation. Probability that a pixel x will be a PS is expressed as,

$$P(x \in PS) = 1 - (1 - \alpha) P_{NPS}(\gamma_x) / P(\gamma_x). \tag{6}$$

After the probability estimation of each candidate pixels, a coherence threshold is set based on percentage of random pixels allowed or fraction of false positives. (Hooper 2006) observed a better coherence threshold using amplitude dispersion. The PS candidate pixels with coherence or γ_x greater than the coherence threshold are classified as PS pixels. Partial PS pixels, which are stable in some interferograms, are “weeded” out based on maximum γ_x among neighbourhood PS pixels.

Deformation Estimation

The deformation estimation ($\varphi_{defo,x,i}$) is the final step of PSInSAR. Once the PS pixels are known, all other phase pixels are removed from wrapped phase interferograms. This is performed before phase unwrapping.

Phase unwrapping is carried out in both temporal and spatial domain to the gridded interferogram. First, the wrapped phase interferograms are re-sampled to gridded interferograms. Then the gridded interferograms are filtered and interpolated using a nearest-neighbour method. The phase differences between neighbouring pixels are then smoothed and unwrapped in time. The outputs of the previous step are used to unwrap the interferograms spatially using maximum a posteriori probability (MAP). After the phase is unwrapped, the unwrap phase contains spatially-correlated look-angle error, atmospheric, and orbit inaccuracy, which tend to mask the $\varphi_{defo,x,i}$ or deformation phase. The look-angle error is estimated in a least-square

sense using correlation with perpendicular baseline. Master contributions for atmosphere and orbit errors are temporally correlated. StaMPS uses low-pass filtering in the time domain to remove master contribution of atmospheric and orbital errors. Atmosphere correction can be removed by high-pass filtering in the time domain which is an optional step.

SBAS Processing

The traditional SBAS method works on multi-looked small baseline interferograms. To reduce the effect of decorrelation, StaMPS's SBAS minimises perpendicular, temporal, and Doppler baselines between two acquisitions. The interferometric pairs are selected such that their coherence values are greater than a predefined coherence threshold. This minimum coherency threshold will generate a small baselines interferometric network with no isolated clusters i.e. connected graph. The SBAS interferograms are formed after the resampled SLCs are filtered in both azimuth and range to maximise correlation. Geometric phase correction is performed on SBAS interferograms using orbit and DEM. The SBAS pixels are sometimes called Slowly-Decorrelating Filtered Phase (SDFP) pixels (Hooper 2008). The selections of SDFP pixels are similar to PS pixels, but here a difference of amplitude dispersion $D_{\Delta A} = \sigma_{\Delta A} / \mu_A$ is used, where $\sigma_{\Delta A}$ is the ratio of standard deviation of the difference in amplitude between master and slave, and μ_A represents mean amplitude. (Hooper 2008) showed that $D_{\Delta A}$ works better than D_A in the case of filtered phase. We used a $D_{\Delta A}$ threshold (0.6) to select a initial set of SDFP pixels. The selection of SDFP pixels is similar to spatial correlation PS algorithm mentioned in PSInSAR processing. The remaining steps are also similar to PS processing. SBAS helps to remove the 3D phase unwrapping errors using residual phase between the unwrapped phase of small baseline interferograms and phase of the single master model to spot the spatially correlated phase jumps. In our case, we converted the LOS displacement of SB network to single-master (SM) network for time-series comparison with PSInSAR.

Results and Analysis

We applied both PSInSAR and SBAS to the same area of Las Vegas using 44 ERS images during 1992–2000 to produce the annual LOS displacement rate and time-series of PSInSAR and SBAS. We chose a threshold of $D_A = 0.4$ for PSInSAR and $D_{\Delta A} = 0.6$ for SBAS. In both cases, pixels were selected based on their temporal coherency and by allowing 20 and 2 random noise pixels per square km in PS and SBAS respectively. A phase noise standard

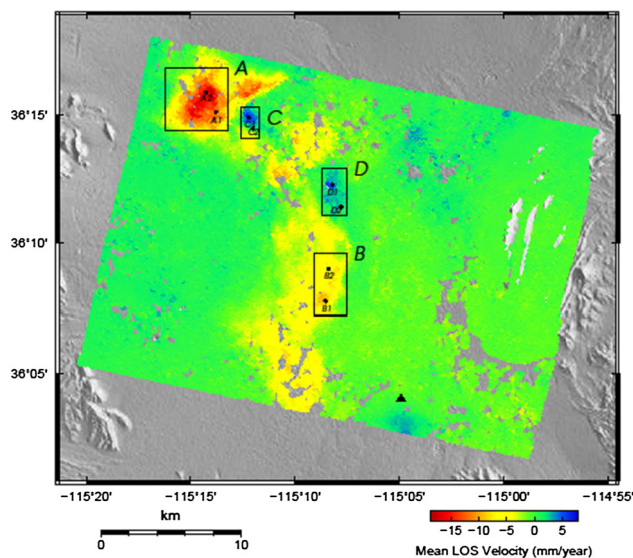


Fig. 5 Annual LOS deformation rate (mm/yr) of Las Vegas (track 356, frame 2871) measured by PSInSAR during 1992–2000 superimposed on SRTM DEM with lat/lon axes. The major areas with ground deformation are represented in black rectangles (A, B, C, and D). The spatial reference point is shown in black triangle (colour figure online)

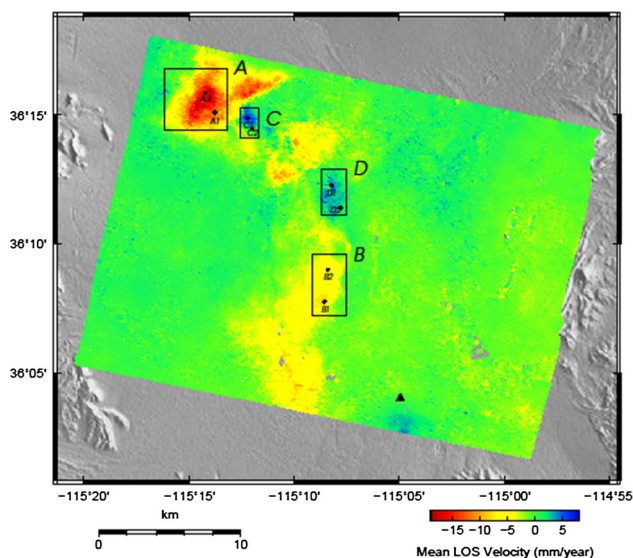


Fig. 6 Annual LOS deformation rate (mm/yr) of Las Vegas (track 356, frame 2871) measured by SBAS during 1992–2000 superimposed on SRTM DEM

deviation of 1 rad was chosen in case of PS. PS pixels were resampled to a grid of 100 m to reduce the effect of noise and to help 3D phase unwrapping. Using PSInSAR, 54510 PS pixels were selected, which was 75773 in the case of SBAS. The number of SDFP pixels is greater than the PS pixels due to more numbers of partially-stable distributed scatterers than dominating scatterers in our study area.

Figures 5 and 6 show the mean LOS velocity (MLV) map of Las Vegas (track 356, frame 2871) during

1992–2000 using PSInSAR (left) and SBAS (right). Positive LOS velocity (mm/yr) indicates that the ground movement towards satellite line of sight, whereas negative LOS velocity shows subsidence or moving away from satellite LOS. The deep red and blue colour indicate the ground areas which are subsided (–ve LOS velocity) and uplifted (+ve LOS velocity) respectively. We found mean LOS velocity for PSInSAR and SBAS lies within the range of –19 to 8 mm/year w.r.t the reference area in the south, depicted in the black triangle. The mean deformation range is taken as 99-percentile to prevent the outliers from swamping the final deformation rate. The magnitude and location of deformation estimated using these methods are in good correlation. Both PSInSAR and SBAS detect major ground deformation in our area.

Comparison Between PS and SBAS

The ground areas with noticeable deformation are represented as black rectangles A, B, C and D in Figs. 5 and 6. We observed subsidence at region A and B and upliftment at region C and D. The subsidence areas located in the north-west and middle part of our study area, A and B, show a MLV of –10.2 and –7.1 mm/year respectively. The upliftment regions in the northern part, C and D, of the city show a MLV of 3.1 and 2 mm/year. We computed the MLV distribution histogram for both PSInSAR and SBAS, shown in Figs. 7 and 8. The histograms are very similar in terms of mean and variance. Most of the PS and SDFP pixels are located around zero MLV, which tells MLV is zero for most of our study region.

For more detailed comparison between PS and SDFP pixels, we computed the common or overlapping pixels between these two methods and found 40,583 common

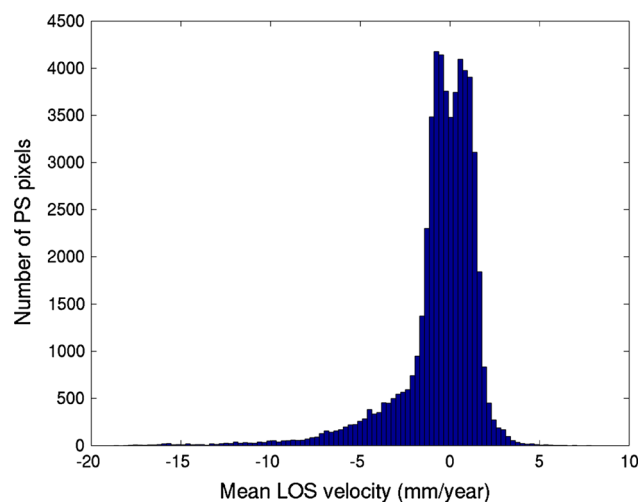


Fig. 7 Histogram of mean LOS displacement rate using PSInSAR generated using 44 ERS images

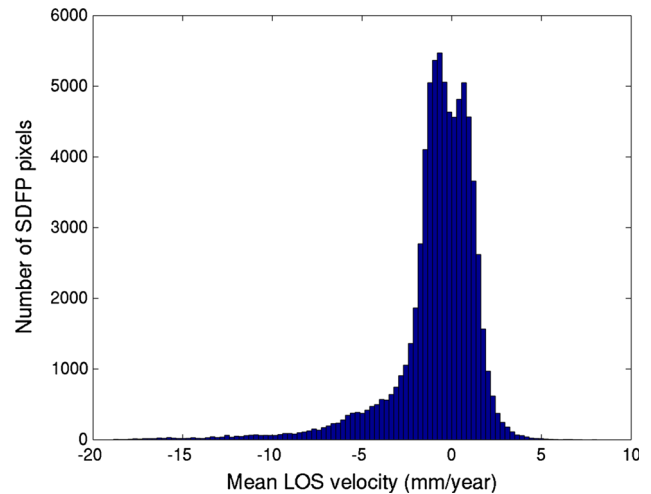


Fig. 8 Histogram of mean LOS displacement rate using SBAS generated using 44 ERS images

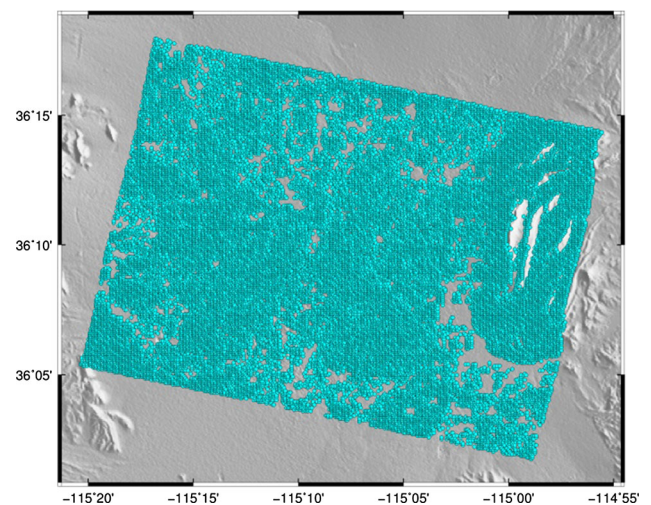


Fig. 9 Common pixels selected between PSInSAR and SBAS are shown in blue. The 40,583 overlapping pixels are overlaid on a SRTM DEM (colour figure online)

pixels in our case, shown in Fig. 9. We used statistical comparison of these pixels for further analysis. In Fig. 10, a scatter plot of MLV between PSInSAR and SBAS was generated using common pixels. We calculated the RMSE as 0.7557, and mean absolute error (MAE) as 0.5549 mm/year. A linear regression line, $y = 0.9438 \times -0.2003$, is fitted to the data. We measured the R-squared value of 0.8962 from our fit and the correlation coefficient of 0.9467, which suggest a good linear relationship between PS and SBAS measurements. However, this analysis does not show a perfect correlation due to some random noise which was not captured during processing. We created a difference MLV histogram between these PS and SDFP common pixels as shown in Fig. 11. The mean of MLV differences is 0.17, which is close to zero, and a low

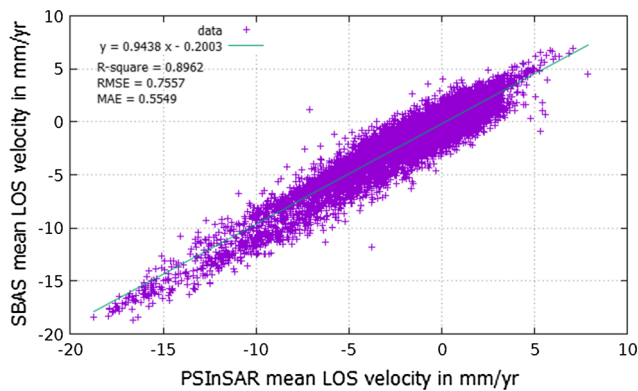


Fig. 10 Scatter plots of 40,583 common PS/SDFP pixels. Linear regression line was fitted to the data

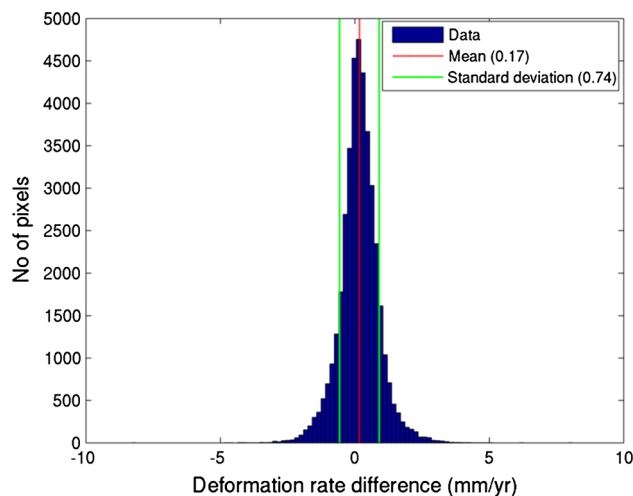


Fig. 11 Distribution of mean displacement rate difference between PSInSAR and SBAS

standard deviation of 0.74 suggests the data is not dispersed. So, the majority of these pixels show almost equal displacement rate with a low standard deviation.

We also compared the estimated time-series between PS and SBAS in addition to the MLV comparison. We selected total eight points A1, A2, B1, B2, C1, C2, D1, and D2, two points each from the region A, B, C, and D shown in Fig. 5 and Fig. 6. The time-series for eight points are generated using mean LOS displacement of all PS or SDFP points selected around 500 m of each point. In all the cases, we chose master as the temporal reference i.e. zero displacement for master. The spatial reference is same as previous. In Figs. 12, 13, 14 and 15, the PSInSAR and SBAS time-series of points A1, A2, B1 and B2 are plotted in red and blue along with error bars which represent the standard deviation of displacement of all PS/SDFP points around 500 m. These four points inside rectangle A and B show subsidence at a rate of -10.169 mm/year (PSInSAR), -11.593 mm/year (SBAS), -14.389 mm/year

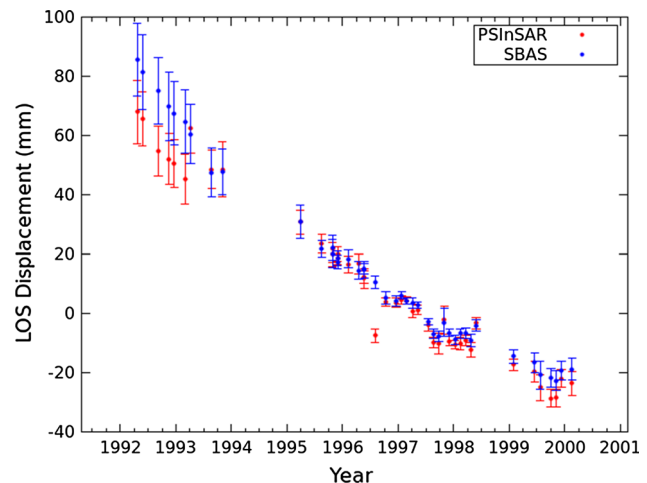


Fig. 12 Estimated LOS deformation time-series of point A1 using the PSInSAR and SBAS method. The PSInSAR and SBAS observations are shown in red and blue respectively. The error bars denote the standard deviation of LOS displacement of PS/SBAS points within 500 m of A1 (colour figure online)

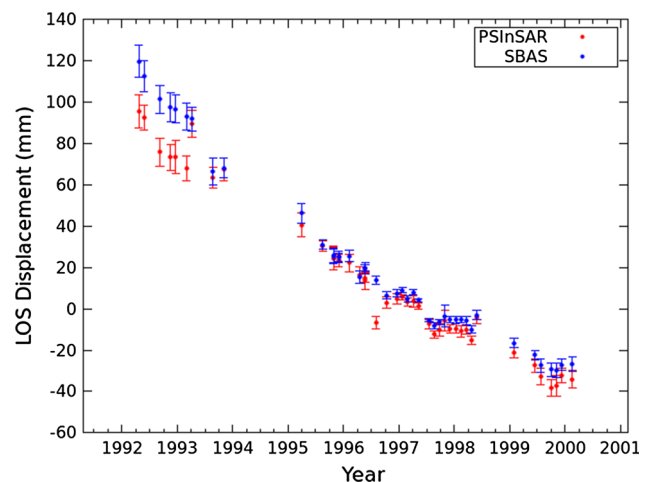


Fig. 13 Estimated LOS deformation time-series of point A2 using the PSInSAR and SBAS method. The PSInSAR and SBAS observations are shown in red and blue respectively. The error bars denote the standard deviation of LOS displacement of PS/SBAS points within 500 m of A2 (colour figure online)

(PSInSAR), -16.242 mm/year (SBAS), -7.087 mm/year (PSInSAR), -6.076 mm/year (SBAS), -6.1 mm/year (PSInSAR), -5.774 mm/year (SBAS). Figures 16, 17, 18 and 19 represent the LOS displacement time-series of points C1, C2, D1, and D2, at deformation rates of 3.075 mm/year (PSInSAR), 4.766 mm/year, -0.272 mm/year (PSInSAR), -0.805 mm/year (SBAS), 2.877 mm/year (PSInSAR), 3.069 mm/year (SBAS), 1.107 mm/year (PSInSAR), 1.638 mm/year (SBAS) respectively. The points inside C and D show a positive displacement rate or upliftment. The mean LOS displacement rates of these

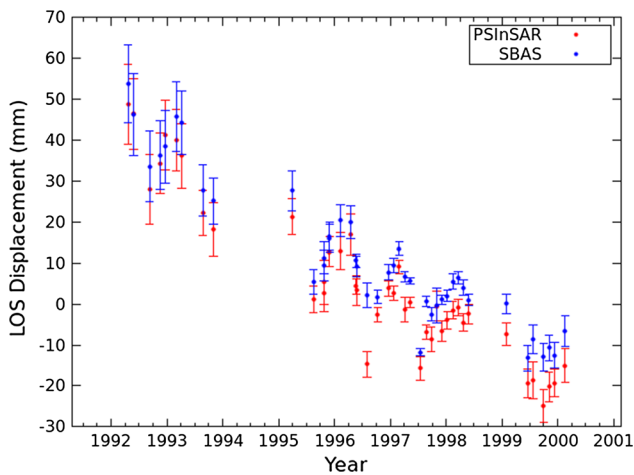


Fig. 14 Estimated LOS deformation time-series of point B1 using the PSInSAR and SBAS method. The PSInSAR and SBAS observations are shown in red and blue respectively. The error bars denote the standard deviation of LOS displacement of PS/SBAS points within 500 m of B1 (colour figure online)

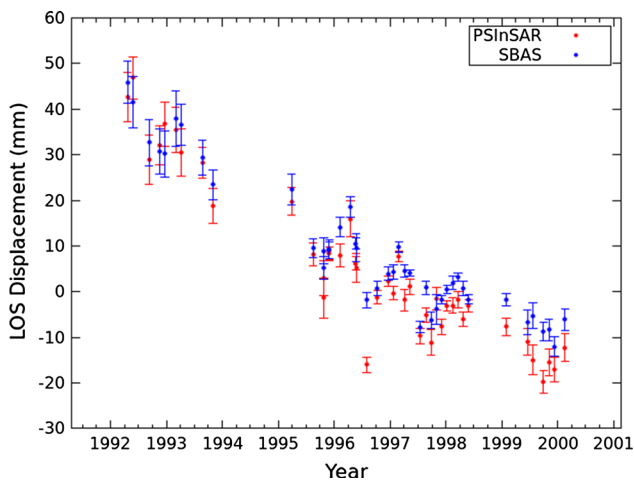


Fig. 15 Estimated LOS deformation time-series of point B2 using the PSInSAR and SBAS method. The PSInSAR and SBAS observations are shown in red and blue respectively. The error bars denote the standard deviation of LOS displacement of PS/SBAS points within 500 m of B2 (colour figure online)

points are shown in Table 3. We calculated the RMSE of 1.1 mm/year between PSInSAR and SBAS observations. We observe the magnitudes and trends of LOS displacement time-series of A, B, C and D using PSInSAR and SBAS are similar. The large magnitude error bars are present in all plots during 1992–1994, probably caused by the interferograms with large baselines which introduce more noisy PS/SDFP pixels during processing. The noisy PS/SDFP pixels introduce phase unwrapping errors which could result in more variance between PSInSAR and SBAS time-series.

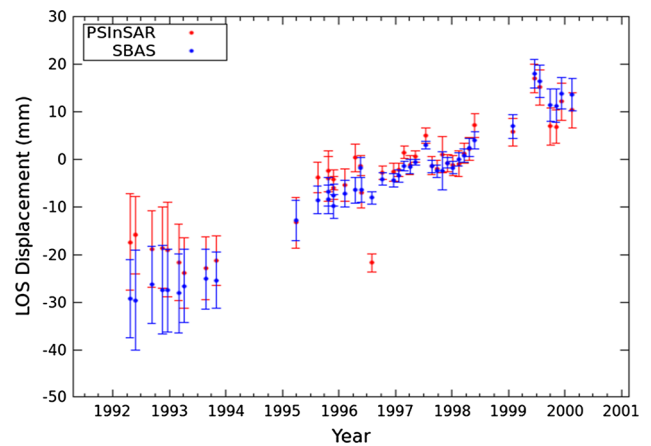


Fig. 16 Estimated LOS deformation time-series of point C1 using the PSInSAR and SBAS method. The PSInSAR and SBAS observations are shown in red and blue respectively. The error bars denote the standard deviation of LOS displacement of PS/SBAS points within 500 m of C1 (colour figure online)

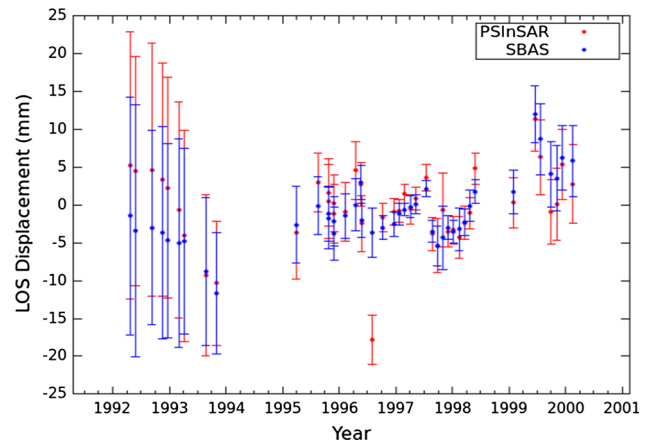


Fig. 17 Estimated LOS deformation time-series of point C2 using the PSInSAR and SBAS method. The PSInSAR and SBAS observations are shown in red and blue respectively. The error bars denote the standard deviation of LOS displacement of PS/SBAS points within 500 m of C2 (colour figure online)

Comparison Between PS-SBAS Time-Series and Ground Water Data

Finally, we compared the InSAR LOS displacement time-series with ground water level depth of two USGS stations, PZD (36.2361, 115.2405) and LVVWD-W028 (36.2246944, -115.2342778) during 1992–2000 to further validate our PSInSAR and SBAS results. The USGS water stations are located in north-west part of Las Vegas. In Figs. 20 and 21, we plotted the InSAR mean LOS displacements of nearest PS and SBAS point within 500 m of ground water station USGS-PZD. The estimated LOS ground displacement using PSInSAR and SBAS are shown in blue asterisks, whereas the green lines denote the ground

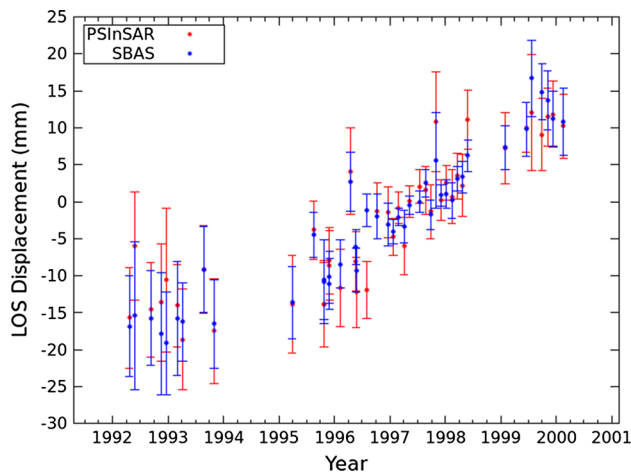


Fig. 18 Estimated LOS deformation time-series of point D1 using the PSInSAR and SBAS method. The PSInSAR and SBAS observations are shown in red and blue respectively. The error bars denote the standard deviation of LOS displacement of PS/SBAS points within 500 m of D1 (colour figure online)

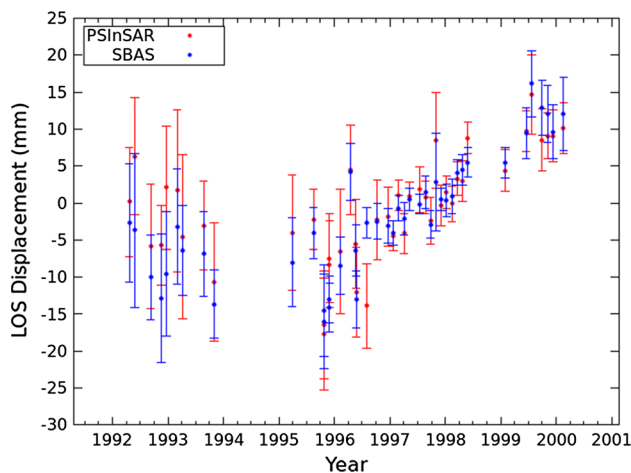


Fig. 19 Estimated LOS deformation time-series of point D2 using the PSInSAR and SBAS method. The PSInSAR and SBAS observations are shown in red and blue respectively. The error bars denote the standard deviation of LOS displacement of PS/SBAS points within 500 m of D2 (colour figure online)

water level USGS-PZD. Although their magnitudes (mm and feet) are not comparable, we observed a similar trend or pattern of ground deformation measured by InSAR and ground water data. The ground water level during December 1994 to September 1997 fell from 290 feet to 324 feet (i.e., -34 feet), and the LOS subsidence values measured by PSInSAR and SBAS at the same time are 4 mm and 6 mm respectively. Following that period, the water level fell from 270 to 307 feet from June 1998 to October 1999 and then rose to 255 feet during October 1999 to February 2000. The subsidence value from June 1998 to October 1999 is 3 and 1 mm for PSInSAR and SBAS respectively. InSAR time-series also show an upliftment (3 mm for PS and 2 mm for SBAS) during October 1999 to February 2000. We inspected InSAR time-series using another USGS ground water station LVVWD-W028 along this study as shown in Figs. 22 and 23. In Figs. 22 and 23, PSInSAR and SBAS estimated LOS ground displacement observations are shown in blue asterisks, whereas, the green lines denote the ground water level of LVVWD-W028 from 1993 to 2000. The water level rose from 288 feet to 216 feet during March 1993 to March 2000. The PSInSAR and SBAS time-series follow the same upliftment pattern during the same time. The upliftment values measured by PSInSAR and SBAS are 9 and 14 mm from Figs. 22 and 23. We can see, in both the cases, the two methods PSInSAR and SBAS show a good correlation with ground water data. Because of the low temporal sampling rate of InSAR, we cannot see an explicit match with ground water level time-series. The discrepancies between the InSAR and ground water levels may be due to phase unwrapping errors, slave atmospheric contributions.

Conclusions

Cross-comparison between StaMPS PSInSAR and validation with ground water data show that PSInSAR and SBAS successfully detect the ground deformation of Las Vegas

Table 3 Comparison between estimated time-series using PSInSAR and SBAS for 8 points in Las Vegas

Point name	PSInSAR (mm/yr)	SBAS (mm/yr)	Difference between PSInSAR and SBAS (mm/yr)	RMSE
A1	-10.169	-11.593	1.424	1.1 mm/yr
A2	-14.389	-16.242	1.853	
B1	-7.087	-6.706	-0.381	
B2	-6.100	-5.774	-0.326	
C1	3.075	4.766	-1.691	
C2	-0.272	-0.805	0.533	
D1	2.877	3.069	-0.192	
D2	1.107	1.638	-0.531	

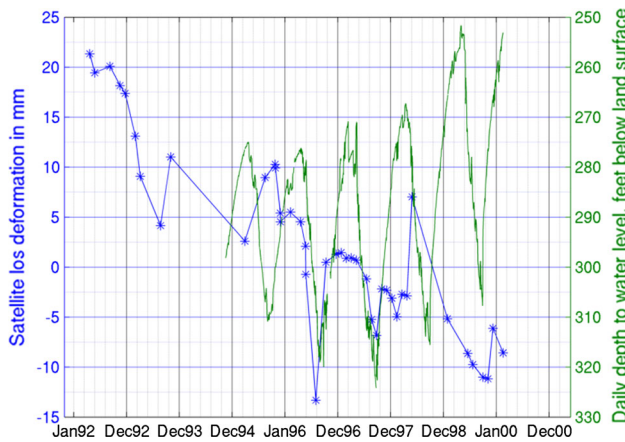


Fig. 20 Comparison of PSInSAR LOS deformation with ground water level data of USGS station PZD. The blue colour denotes the PSInSAR measured LOS displacement in mm, whereas the green colour is the ground water level in feet (colour figure online)

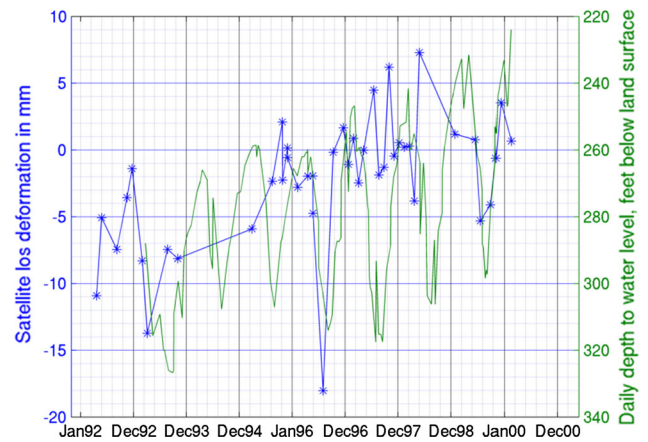


Fig. 22 Comparison of LOS displacement measured by PSInSAR with ground water level of USGS data of station LVVWD-W028. The blue colour denotes the PSInSAR measured LOS displacement in mm, whereas the green colour is the ground water level in feet (colour figure online)

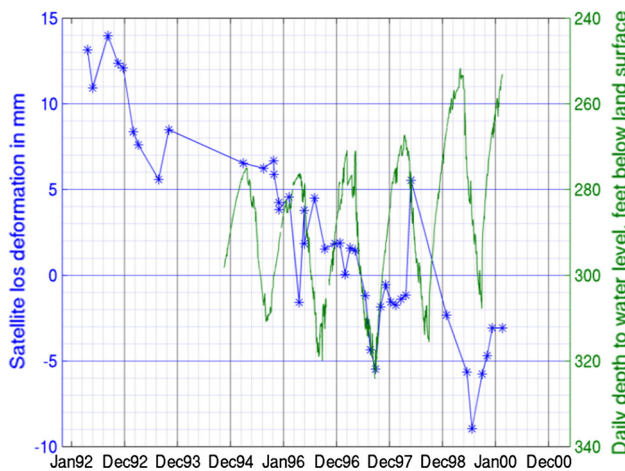


Fig. 21 Comparison of SBAS LOS deformation with ground water level data of USGS station PZD. The blue colour denotes the SBAS measured LOS displacement in mm, whereas the green colour is the ground water level in feet (colour figure online)

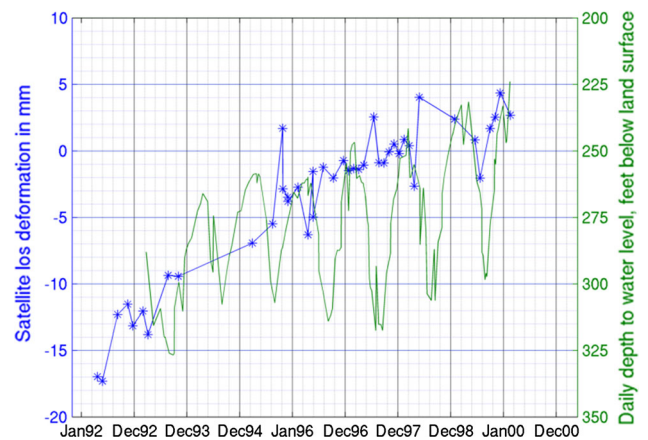


Fig. 23 Comparison of LOS displacement using SBAS with ground water level of USGS data of station LVVWD-W028. The blue colour denotes the SBAS measured LOS displacement in mm, whereas the green colour is the ground water level in feet (colour figure online)

during 1992–2000 using 44 C-band ERS SAR images of descending pass. The mean and RMSE of MLV discrepancy in time-series between PSInSAR and SBAS are 0.68 and 1.1 mm/year respectively. Using PS/SDFP common pixels, the mean and RMSE of MLV discrepancy are 0.17 and 0.75 mm/year. Subsidence and upliftment bowls were observed over the city for the same time-period which correlates with the previous results. The validation of InSAR with ground water data could be improved using GPS displacement data. Validation using GPS data can also give an accuracy of InSAR time-series. The choice of a stable reference point is needed for more precise InSAR time-series analysis. Cross-comparison of InSAR results with other frequency sensors like L-band and X-band will

help us for more robust and accurate deformation detection and estimation. The short revisit time of L and X-band will provide datasets with good coherence. Robust atmospheric corrections for more precise InSAR time-series can be performed using weather models like ERA and WRF.

Acknowledgements The authors would like to thank ESA for providing ERS datasets. We would also like to thank Dr. Andy Hooper for the StaMPS software.

References

Adam, N., Kampes, B., Eineder, M., Worawattanamateekul, J., & Kircher, M. (2003). The development of a scientific permanent

- scatterer system. In *ISPRS Workshop High Resolution Mapping from Space, Hannover, Germany* (Vol. 2003, pp. 6–7).
- Amelung, F., Galloway, D. L., Bell, J. W., Zebker, H. A., & Laczniak, R. J. (1999). Sensing the ups and downs of Las Vegas: InSAR reveals structural control of land subsidence and aquifer-system deformation. *Geology*, 27(6), 483–486.
- Bell, J. W., Amelung, F., Ferretti, A., Bianchi, M., & Novali, F. (2008). Permanent scatterer InSAR reveals seasonal and long-term aquifer-system response to groundwater pumping and artificial recharge. *Water Resources Research*, 44(2), 1–18.
- Berardino, P., Fornaro, G., Lanari, R., & Sansosti, E. (2002). A new algorithm for surface deformation monitoring based on small baseline differential SAR interferograms. *IEEE Transactions on Geoscience and Remote Sensing*, 40(11), 2375–2383.
- Colesanti, C., Ferretti, A., Prati, C., & Rocca, F. (2003). Monitoring landslides and tectonic motions with the permanent scatterers technique. *Engineering Geology*, 68(1), 3–14.
- Ferretti, A., Prati, C., & Rocca, F. (2000). Nonlinear subsidence rate estimation using permanent scatterers in differential SAR interferometry. *IEEE Transactions on Geoscience and Remote Sensing*, 38(5), 2202–2212.
- Ferretti, A., Prati, C., & Rocca, F. (2001). Permanent scatterers in SAR interferometry. *IEEE Transactions on Geoscience and Remote Sensing*, 39(1), 8–20.
- Fu, L.-L., & Holt, B. (1982). Seasat views oceans and sea ice with synthetic aperture radar. *Earth resources and remote sensing* (pp. 3–11): Jet Propulsion Lab., California Institute of Technology.
- Galloway, D., Jones, D. R., & Ingebritsen, S. E. (1999). Land subsidence in the United States. *Circular 1182, US Geological Survey* (pp. 149–150).
- Hanssen, R. F. (2001). *Radar interferometry: data interpretation and error analysis* (Vol. 2, pp. 96–99). Berlin: Springer.
- Hoffmann, J., Zebker, H. A., Galloway, D. L., & Amelung, F. (2001). Seasonal subsidence and rebound in Las Vegas Valley, Nevada, observed by synthetic aperture radar interferometry. *Water Resources Research*, 37(6), 1551–1566.
- Hooper, A. (2006). *Persistent scatter radar interferometry for crustal deformation studies and modeling of volcanic deformation*. Ph.D. thesis, Stanford university, Stanford.
- Hooper, A. (2008). A multi-temporal InSAR method incorporating both persistent scatterer and small baseline approaches. *Geophysical Research Letters*, 35(16), 1–5.
- Hooper, A., Bekaert, D., Spaans, K., & Arkan, M. (2012). Recent advances in SAR interferometry time series analysis for measuring crustal deformation. *Tectonophysics*, 514, 1–13.
- Hooper, A., Segall, P., & Zebker, H. (2007). Persistent scatterer interferometric synthetic aperture radar for crustal deformation analysis, with application to Volcán Alcedo, Galápagos. *Journal of Geophysical Research Solid Earth*, 112(B7), 1–21.
- Hooper, A., Zebker, H., Segall, P., & Kampes, B. (2004). A new method for measuring deformation on volcanoes and other natural terrains using InSAR persistent scatterers. *Geophysical Research Letters*, 31(23), 1–5.
- Kampes, B. M. (2005). *Displacement parameter estimation using permanent scatterer interferometry*. Ph.D. thesis, TU Delft, Delft University of Technology, Netherlands.
- Kampes, B. M., & Adam, N. (2006). The STUN algorithm for persistent scatterer interferometry. In *Fringe 2005 Workshop*. (Vol. 610, pp. 16).
- Lanari, R., Mora, O., Manunta, M., Mallorquí, J. J., Berardino, P., & Sansosti, E. (2004). A small-baseline approach for investigating deformations on full-resolution differential SAR interferograms. *IEEE Transaction on Geoscience and Remote Sensing*, 42(7), 1377–1386.
- Ng, A. H.-M., Ge, L., Li, X., & Zhang, K. (2012). Monitoring ground deformation in Beijing, China with persistent scatterer SAR interferometry. *Journal of Geodesy*, 86(6), 375–392.
- Tesauro, M., Berardino, P., Lanari, R., Sansosti, E., Fornaro, G., & Franceschetti, G. (2000). Urban subsidence inside the city of Napoli (Italy) observed by satellite radar interferometry. *Geophysical Research Letters*, 27(13), 1961–1964.
- Van der Kooij, M., Hughes, W., Sato, S., & Poncos, V. (2005). *Coherent target monitoring at high spatial density: examples of validation results*. In Fringe Workshop, European Space Agency.
- Werner, C., Wegmüller, U., Strozzi, T., & Wiesmann, A. (2003). Interferometric point target analysis for deformation mapping. In: *Geoscience and remote sensing symposium, 2003. IGARSS'03. Proceedings. 2003 IEEE international*. (Vol. 7, pp. 4362–4364) IEEE.
- Zebker, H. A., & Villasenor, J. (1992). Decorrelation in interferometric radar echoes. *IEEE Transactions on Geoscience and Remote Sensing*, 30(5), 950–959.